

Supporting Information

Ohn et al. 10.1073/pnas.1605737113

SI Methods

Animals. C57BL/6 mice of either sex were used for hair cell physiology and morphology at p14–20 (Figs. 1–4). *Ca_v1.3^{HA/HA}* mice (36) and littermate controls were provided by Jörg Striessnig, University of Innsbruck, Innsbruck, Austria, and used at p14–18 (patch clamp) and 6–8 wk (in vivo). *Dfcr* mice (46), Jax (Balb/C background), and littermates were used at p14–17. *Gipc3* mutants (48) were compared with age-matched C57BL/6 at p14–27 (19).

Patch Clamp and Confocal Ca²⁺ Imaging. Apical cochleae (first 2/3 turns) were freshly dissected. Inner border cells and phalangeal cells were gently removed by a suction pipette, exposing an IHC basolateral membrane. The patch pipette solution contained (in millimolar) 123 Cs-glutamate, 1 MgCl₂, 1 CaCl₂, 10 EGTA, 13 tetraethylammonium (TEA)-Cl, 20 Hepes, 2 MgATP, and 0.3 NaGTP (pH 7.3). For live imaging, it contained the Ca²⁺ indicator Fluo-8FF (0.8 mM; AAT Bioquest) and the TAMRA-conjugated CtBP2/RIBEYE-binding dimer peptide (20 μM; Biosynthon). For Fig. S5, we used 111 mM L-glutamate, 4 mM MgATP, 1 mM glutathione, 0.8 mM Fluo-4FF penta-K⁺ salt (Life Technologies), and 10 μM TAMRA-conjugated CtBP2/RIBEYE-binding dimer peptide. IHCs were continuously superfused with an extracellular solution containing (in millimolar) 102.2 NaCl, 2.8 KCl, 1 MgCl₂, 5 CaCl₂, 35 TEA-Cl, 10 Hepes, and 2 g/L glucose (pH 7.2). An EPC-10 amplifier and Patchmaster software (HEKA Elektronik) were used and Ca²⁺ influx was evoked by step depolarizations from −87 mV to −7 mV or ramp depolarizations from −87 mV to 63 mV. All voltages were corrected for liquid junction potential (17 mV) and voltage drops across series resistance (*R_s*). IHCs were held at −87 mV. Recordings were discarded when holding current exceeded 50 pA, *R_s* exceeded 10 MΩ within 4 min after break-in, or rundown of Ca²⁺ current exceeded 25%. Ca²⁺ imaging was performed with a spinning disk confocal scanner (CSU22; Yokogawa) mounted on an upright microscope (Axio Examiner; Zeiss) with 63×, 1.0 N.A. objective (W Plan-Apochromat; Zeiss). Images were acquired by a back-illuminated CCD camera with 80 × 80 pixels within a 19.2 × 19.2-mm CCD chip (NeuroCCD; Redshirt Imaging) or a scientific complementary metal-oxide-semiconductor camera (Neo; Andor). Ca²⁺ indicators and TAMRA-conjugated peptide were excited by diode-pumped solid-state lasers with 491-nm and 561-nm wavelength, respectively (Cobolt AB). The spinning disk was set to 2,000 rpm to synchronize with the 10-ms acquisition time of the camera. Using a piezo positioner for the objective (Piezosystem), focal planes were acquired in an order randomized in each cell to avoid systematic effects of fluorophore bleaching. *C_m* measurements were performed as previously described (69) and exocytic *C_m* changes calculate from the difference of *C_m* before and after the depolarization (400 ms, skipping the initial 40 ms).

Immunohistochemistry and Confocal Imaging. The organ of Corti apical 2/3 turn was prepared for “whole-mount” imaging as described in ref. 70, but the protocol was modified after the secondary antibody rinse. The following primary antibodies were used: goat anti-CtBP2 (1:150; Santa Cruz Biotechnology), mouse anti-GluA2 (1:75; Millipore), rabbit anti-*Ca_v1.3* (1:75; Alomone Labs), mouse anti-bassoon SAP7F407 (Abcam), rabbit anti-BK_{Ca} (1:200; Alomone Labs), and mouse anti-otoferrin (1:300; Abcam). Secondary antibodies used were Alexa Fluor 488-conjugated antimouse, Alexa Fluor 596-conjugated anti-goat, and Alexa Fluor 647-conjugated anti-rabbit IgG antibodies (1:200; Invitrogen).

For improved structural preservation, 50-μm-thick plastic film was taped to the glass surface on either side of the sample to act as spacers, preventing overflattening of the whole-mount. To minimize differences in attenuation at different focal depths, tissue was embedded in 2,2′-thiodiethanol (71). To control for artifactual differences between synapses due to bleaching and attenuation of the optical signal resulting from order of acquisition and synapse position, respectively, we mounted the tissue between two coverslips. This allowed for imaging the same field of IHCs with either the apical surface or the basilar membrane surface oriented toward the objective of the Leica SP5 confocal microscope (Fig. S3). Data pooled from multiple volumes were acquired with identical settings. For display in Fig. 1C the projections were made from optical sections deconvolved with a model of the optical point spread function using the Richardson–Lucy algorithm in ImageJ software, with default settings and the pixel dimensions, emission wavelength, and numerical aperture of the experiments.

Extracellular Recordings from Auditory Nerve Fibers. Single unit recordings from mouse SGNs were performed as described (4, 70). In brief, mice were anesthetized by i.p. injection of urethane (1.32 μg/g), xylazine (5 μg/g), and buprenorphine (0.1 μg/g), and parts of the occipital bone and cerebellum were removed to expose the anteroventral cochlear nucleus (AVCN). Sound-responsive single neurons were identified based on spontaneous and noise-induced action potential firing and a basic characterization was performed by measuring their spontaneous rate, tuning curve, and poststimulus time histograms. SGNs were discriminated from primary neurons of the AVCN by their discharge pattern, first spike latency, and stereotaxic position. Recordings and offline analysis using waveform-based spike detection were performed using custom-written MATLAB software (The MathWorks, Inc.) and TDT system III hardware (Tucker-Davis Technologies) and an ELC-03XS amplifier (NPI Electronics).

Data Analysis. Live-imaging and IHC patch-clamp data were analyzed by custom programs in Igor Pro-6.2 (Wavemetrics). The change of Ca²⁺-indicator fluorescence, our proxy of AZ Ca²⁺ influx, was estimated as $\Delta F/F_0$, where *F*₀ is the fluorescence intensity at −87 mV and ΔF is the difference when depolarized to −7 mV (steps) or variable potentials (voltage ramps). Ca²⁺-indicator intensity was calculated by the average of nine pixels centered on the pixel showing the greatest fluorescence increase. Maximal $\Delta F/F_0$ was the average of last 40 ms during step depolarizations and five points at the peak $\Delta F/F_0$ during the voltage ramp. To refine the noisy FV traces, we fit the raw traces to the equation $F(V) = F_0 + [G_{\max}(V_r - V)] / (1 + e[(V_h - V)/k])$. The fit was used to calculate the fractional activation curve, dividing it by the extrapolated maximal $\Delta F/\Delta V$ estimated by linear fitting of the decay of fluorescence with voltage. Then, this trace was fitted by a Boltzman function to estimate the *V_h* and slope factor of the Ca²⁺-indicator fluorescence at a given AZ. Synaptic ribbon fluorescence was estimated as the ratio of TAMRA fluorescence to that of the nearby IHC cytoplasm typically eight or nine pixels away (*F_{ribbon}/F_{nearby}*), measuring the pixel with strongest intensity. IHC cytoplasmic volumes were displayed with the plugin “3D viewer” in Fiji software.

To analyze the intensity and position of synapses in confocal images of fixed organ of Corti whole mounts, a customized algorithm was developed as a program in MATLAB software. The

locations of synapses were defined as the centers of mass of fluorescent spots after thresholding by a subjective intensity criterion for each of the three channels. The average voxel intensity in the volume, excluding voxels that exceeded the threshold value, was subtracted as background. Gaussian functions were fitted in three dimensions to determine the center of mass of each cluster. Immunofluorescence intensities were measured on each channel as the sum of the voxel values within a defined region of interest (± 500 , 500 , and 835 nm or ± 10 , 10 , and 2 pixels in X, Y, and Z) with origin at the center of mass of each GluA2-positive cluster. After marking the center of each IHC nucleus, observing the relative orientation of the pre-synaptic ribbon and the postsynaptic receptor array allowed us to assign each synapse to an IHC. The Cartesian coordinates of synapses were transformed to cell-centric cylindrical coordinates to define the cellular axes and to adjust differences in cellular

orientation relative to the XYZ axes of the microscope. Keeping one end of the line centered on the nucleus, the angle of the axis was adjusted once in the XY plane and once in the YZ plane to compensate for the pitch and yaw of each hair cell (Fig. S3). After adjustment, points along the central axis were defined as zero on the tonotopic and modiolar-pillar axes. Intensities of synaptic puncta as a function of position could be analyzed for multiple cells by overlaying their central axes with alignment to the center of each nucleus.

Jitter is presented as SD or SEM, as noted. Two-tailed *t* tests or, if data were not normally distributed and/or variance was unequal between samples, the Wilcoxon rank sum test were used for statistical comparisons between two samples. Box plots show 10, 25, 50, 75, and 90% percentiles; **P* < 0.05, ***P* < 0.01, and ****P* < 0.001.

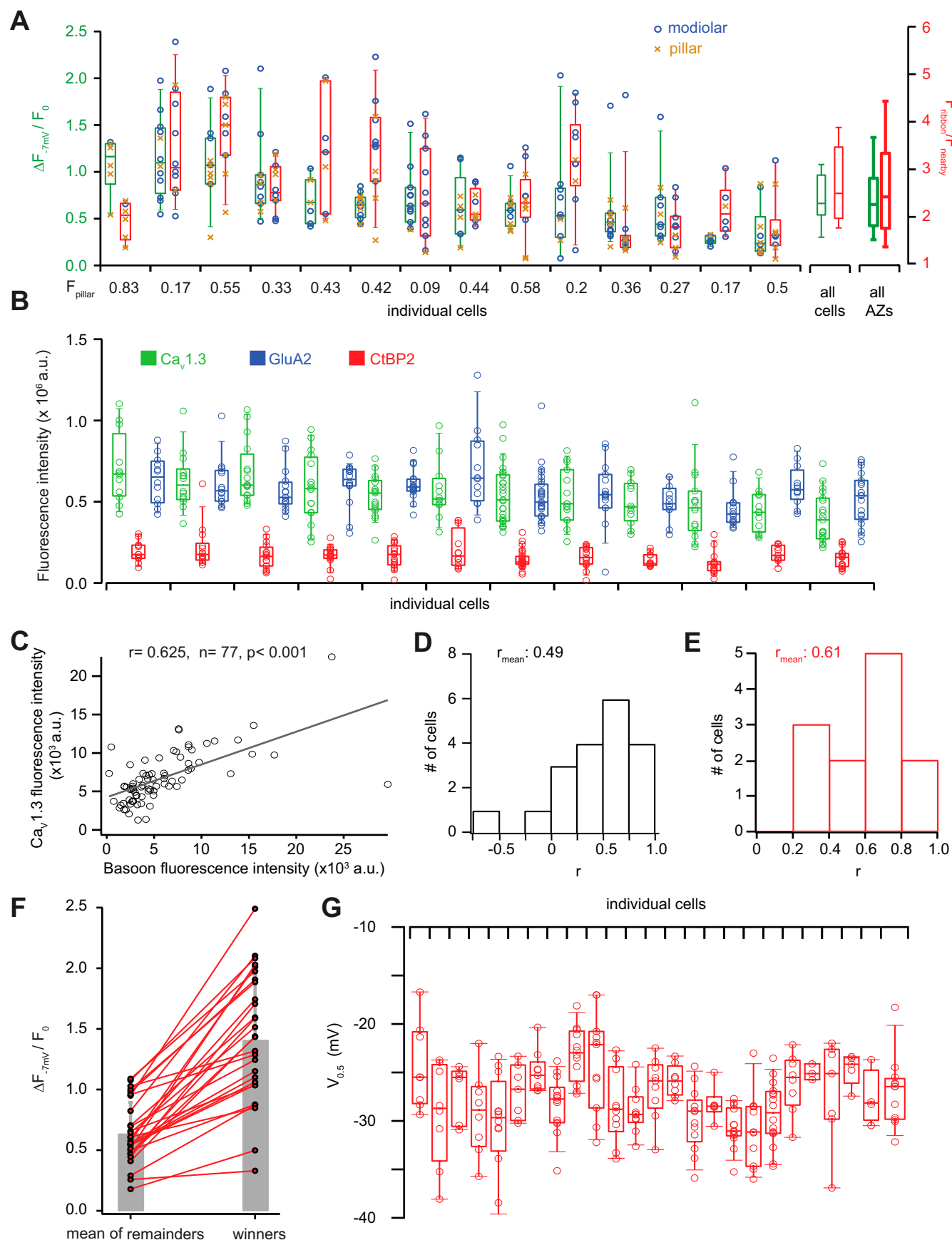


Fig. S1. Quantification of functional and molecular markers of the strength of IHC synapses. (A) Box plots (10, 25, 50, 75, and 90% values) show the statistics of maximal AZ Ca^{2+} influx ($\Delta F_{-7\text{mV}}/F_0$, green) intensity and of RIBEYE-peptide fluorescence (red) of AZs in individual cells (left), of mean $\Delta F_{-7\text{mV}}/F_0$ and mean RIBEYE-peptide fluorescence of all cells (right), and of $\Delta F_{-7\text{mV}}/F_0$ and of RIBEYE-peptide fluorescence all AZs (rightmost) as recorded in the live-imaging experiments. Individual data points are superimposed on the box plots of the individual IHCs, with color coding for modiolar (blue) or pillar (amber) position of the AZ. The number underneath each IHC represents the fraction of pillar AZs. (B) Statistics of the immunofluorescence for all labeled synapses of individual IHCs in the organ of Corti. Box plots display the distributions of the immunofluorescence intensity of presynaptic $\text{Ca}_v1.3$ clusters (green) and RIBEYE/CtBP2-labeled ribbons (red) as well as GluA2-labeled glutamate receptor clusters (blue). Individual data points are superimposed on the box plots of the individual IHCs. (C) Scatter plot of the immunofluorescence intensity of presynaptic $\text{Ca}_v1.3$ clusters and corresponding bassoon immunofluorescence. (D) Correlation of maximal AZ Ca^{2+} influx and RIBEYE-peptide fluorescence within individual IHCs. Histogram displays the distribution of the correlation coefficients of individual IHCs in the live-imaging experiment: The average correlation coefficient among cells in the live-imaging experiment was 0.49. (E) Correlation of $\text{Ca}_v1.3$ and RIBEYE/CtBP2 immunofluorescence within individual IHCs. Histogram displays the distribution of the correlation coefficients of individual IHCs in the immunolabeled organ of Corti. The averaged correlation coefficient among cells was 0.61 in immunohistochemistry. (F) AZ Ca^{2+} influx between the strongest AZ (winners) and the mean of the remaining AZs in individual IHCs. Gray: mean \pm SEM. (G) Box plots and individual values of $V_{0.5}$ of the AZs within individual IHCs.

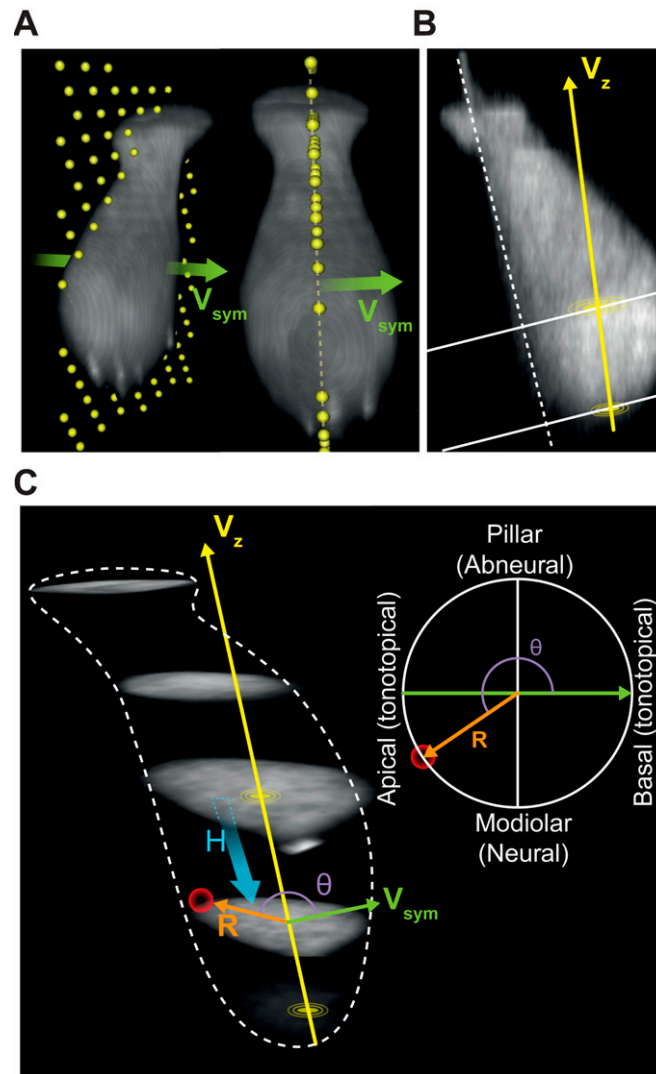


Fig. S2. The method and definition for the reconstruction of hair cell in cylindrical-like coordination system. (A) Three-dimensional images of an IHC from different viewpoints. (Left) The viewpoint from modiolar (tonotopically) basal side. (Right) The viewpoint from modiolar side. The plane containing yellow dots depicts the plane of symmetry of the IHC and the green arrow represents the normal vector of the plane of symmetry (V_{sym}). (B) The plane of symmetry: The white dot line is drawn along the pillar edge of the IHC. The original 3D stack image was sectioned along this line. The yellow disk is the center of the new coordination system, which is the center of mass of the section containing the largest area of cell fluorescence. The central axis V_z connects the origin to the center of mass of the lowest section. (C, Right) The distance of a synapse (the red ball) to the center of mass of the plane containing this synapse. H , distance in height between the plane containing origin to the plane containing the synapse; θ , angle of R to V_{sym} . We identified the plane of symmetry by maximizing mirror symmetry along the orthogonal tonotopic axis (A). Then we sectioned the IHC in a straight line (white dashed line, B) which fits to the pillar edge on the plane of symmetry. The center of mass for each section was estimated and we connected the center of the bottom-most one to the center of the largest section to form the central axis (V_z , B and C). The cylindrical coordinate of each synapse/microdomain was transformed based on the central axis V_z , vector of plane of symmetry V_{sym} , and their cross-product V_{mp} .

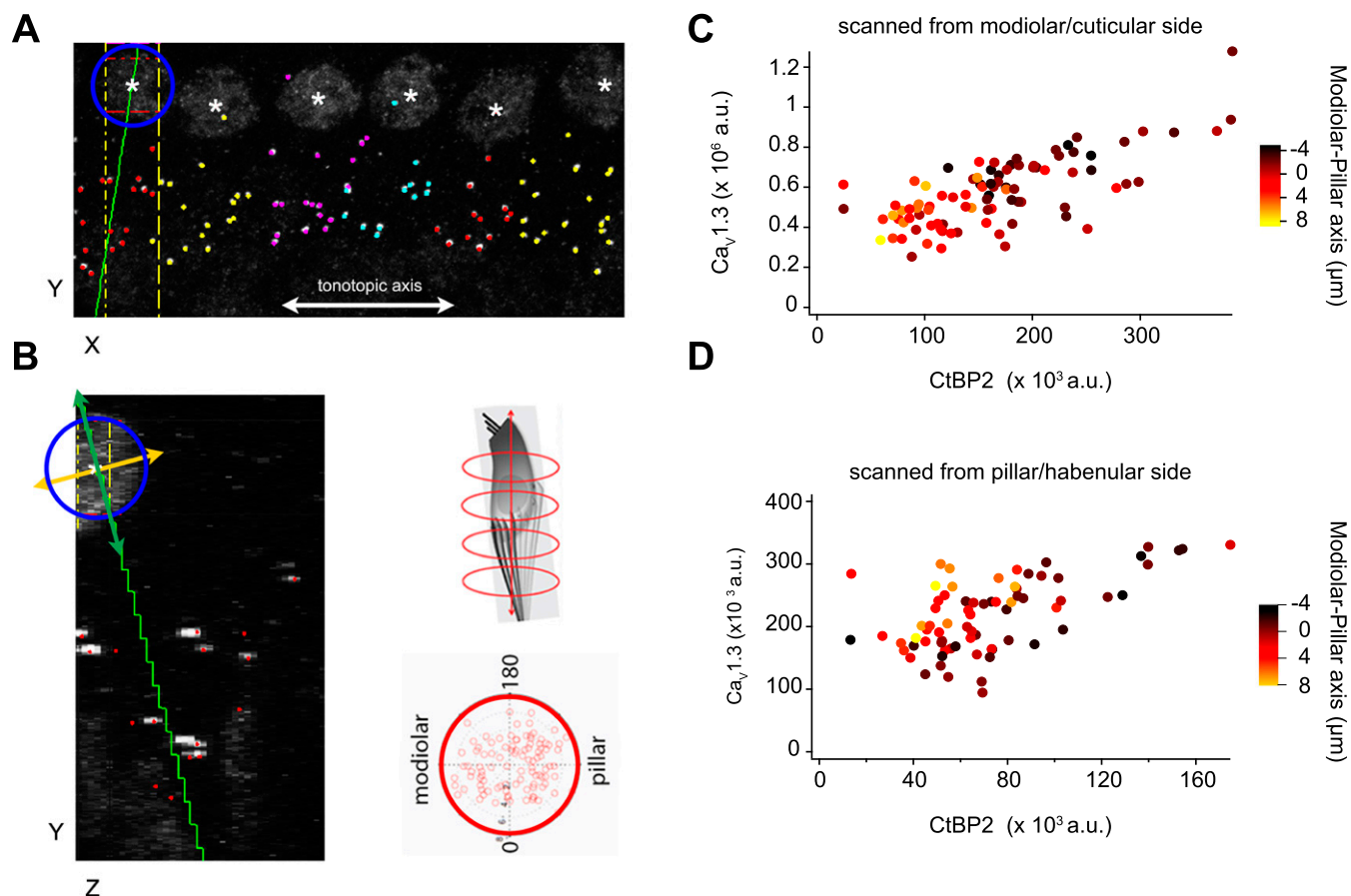


Fig. S3. Analysis of AZ properties by synaptic position on the IHC. (A and B) Multicellular alignment via 3D transformation from Cartesian coordinates of the confocal stack to a cell-centric cylindrical coordinate system, using custom MATLAB routines. For each cell, the nuclear center (white asterisks) was registered in three dimensions using the nuclear immunoreactivity of the CtBP2 antibody. The tonotopic dimension for each image was approximated as the confocal microscope's X dimension (white line in A) by adjusting the rotation of the region of interest. Synapses were sorted by cell, based on proximity to nuclei and orientation of each juxtaposed pre- and postsynaptic pair of CtBP2- and GluA2-labeled puncta. A and B show the CtBP2 channel only. Presynaptic ribbons are marked with dots colored by cell. The center of the nucleus defined one point on a line chosen as the cell's central longitudinal axis. The cell on the left of A (XY plane) has a blue circle around the nucleus. IHCs were visualized individually in the ZY plane by projecting a volume limited along the X axis, within the width of the cell nucleus (yellow vertical lines in A). Synapses belonging to this cell, but positioned outside of the subvolume displayed in the ZY plane, were included as colored markers (red dots without accompanying fluorescence in B). The center of each nucleus was defined as zero on the central longitudinal axis, which extended positively toward the basal pole of the IHC from the direction of the cuticular plate toward the habenula perforata. The second point defining this axis was set by adjusting the axis line in the XY plane (green line in A) and in the ZY plane (green line in B). In the YZ plane, visualizing only the synapses belonging to the cell being analyzed, the axis was chosen based on a user-defined balance of synapses on either side of a line through the nuclear center and through the cluster of synapses at the basal pole. The IHC central longitudinal axis (green) is perpendicular to the defined modiolar–pillar axis in the ZY plane (orange line in B). Using the cell-centric cylindrical coordinates, data from all six cells in the image were overlaid on a projection along the longitudinal axis (polar plot, B, lower right). The longitudinal axis is orthogonal to the plane defined by the perpendicular tonotopic axis (0–180°) and modiolar–pillar axis. (C and D) Synapses with greater $Ca_v1.3$ and CtBP2 fluorescence tended to be positioned toward the modiolar side of the modiolar–pillar axis. In C, the scatter plot is for the six cells shown in A, imaged with the modiolar side toward the objective in a top-down sequence, imaging the modiolar-side synapses first. In D, the scatter plot is for the same six cells imaged with opposite orientation of the specimen, to control for potential artifacts due to optical attenuation and bleaching. The modiolar-side synapses closer to the coverslip and imaged first in C were further from the coverslip and imaged last in D. A similar relationship was observed in each case, showing that modiolar synapses tended to have more immunofluorescence for $Ca_v1.3$ and CtBP2.

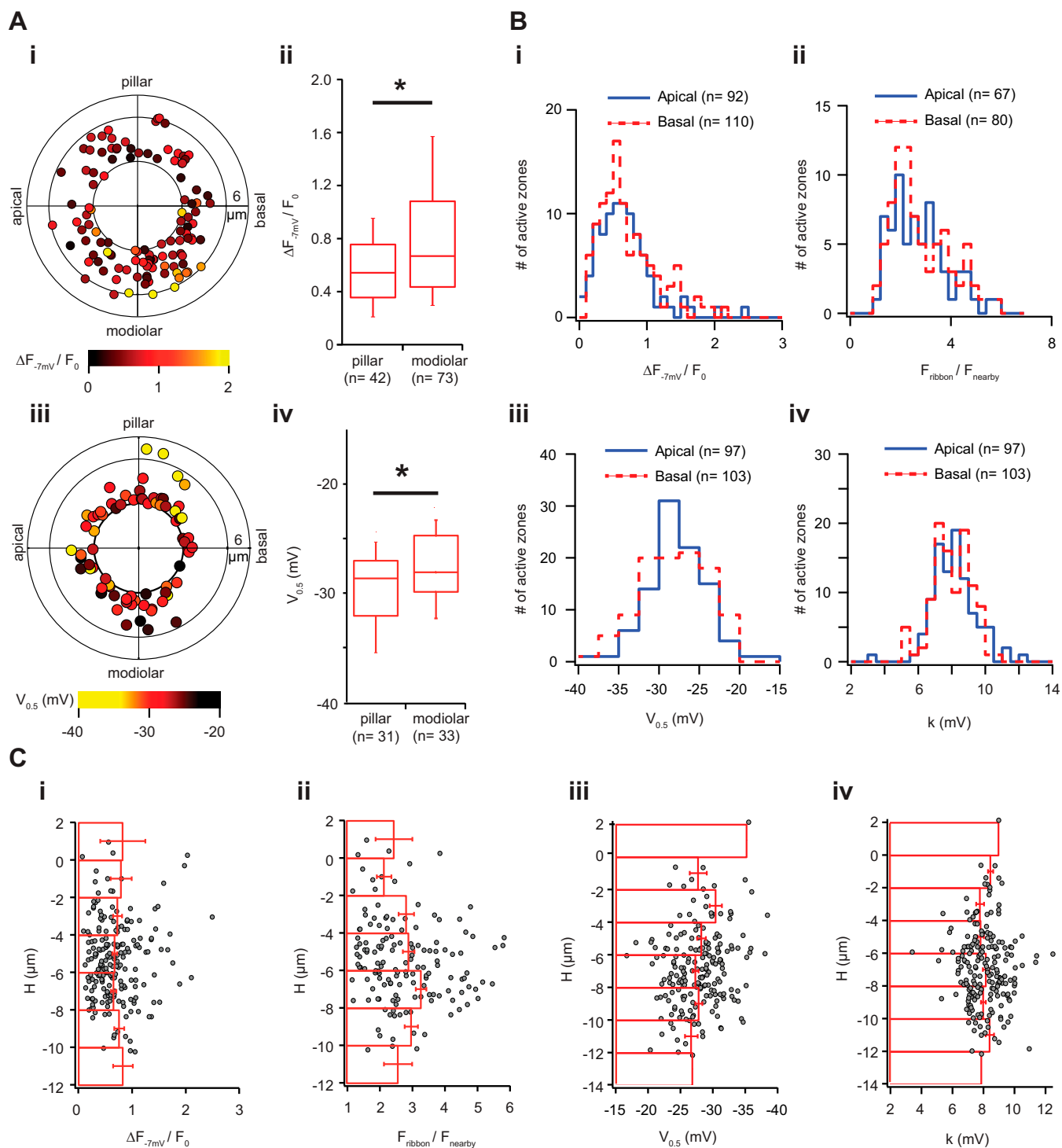


Fig. S4. AZ properties as a function of position within the IHC. (A) Spatial distribution of maximal AZ Ca^{2+} influx ($\Delta F_{-7mV}/F_0$) without the basal cap. (i) Polar chart displays $\Delta F_{-7mV}/F_0$ as a function in position, when AZ were projected along the central axis. In contrast to Fig. 2A, we removed AZs with a radius smaller than $3 \mu m$, which are mostly located on the basal end of IHC ($n = 115$) and pose a challenge to assign to one of the sectors. (ii) Box plots describe the distribution of $\Delta F_{-7mV}/F_0$ of modiolar and pillar halves. The AZs on the modiolar half had significantly stronger $\Delta F_{-7mV}/F_0$ than those on the pillar half. (iii) Polar chart displays $V_{0.5}$ as a function in position, when AZ were projected along the central axis. In contrast to Fig. 4A, we removed AZs with a radius smaller than $3 \mu m$, which are mostly located on the basal end of IHC and pose a challenge to assign to one of the sectors. (iv) Box plots describe the distribution of $V_{0.5}$ on modiolar and pillar halves. The AZs of the pillar half had significantly more hyperpolarized $V_{0.5}$ than those of the modiolar side. (B) No obvious gradients of synaptic properties along the tonotopic axis. (i) The distributions of maximal AZ Ca^{2+} influx ($\Delta F_{-7mV}/F_0$), (ii) intensity of RIBEYE-peptide fluorescence, (iii) $V_{0.5}$, and (iv) k in both tonotopical apical (low-frequency) and basal (higher-frequency) sides of IHCs. There are no significant statistical differences observed between these two sides in all four measured parameters (Wilcoxon rank sum test). (C) No obvious gradients of synaptic properties along the longitudinal axis. This figure shows the spatial arrangements of (i) maximal AZ Ca^{2+} influx ($\Delta F_{-7mV}/F_0$), (ii) the intensity of RIBEYE-peptide fluorescence, (iii) $V_{0.5}$, and (iv) k along the longitudinal axis of the IHC. The 0 layer of the H position corresponds to the plane with the largest IHC cross-section on the axis V_z (Fig. S2). Positive H values indicate an AZ position closer to cuticular plate, and negative closer to the basal pole. Red bars in this figure represent the mean and SD of the corresponding quantity in their specified longitudinal positions.

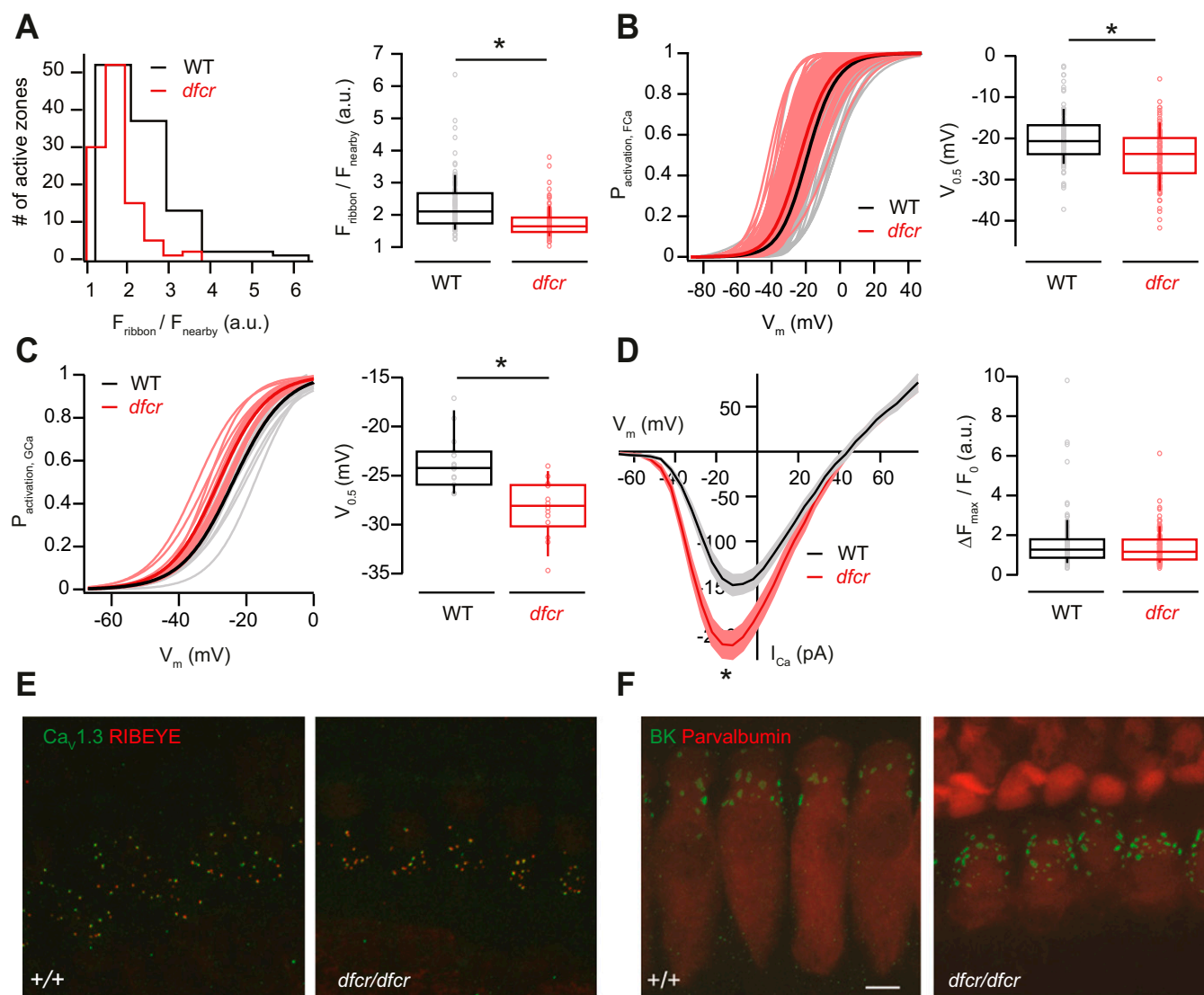
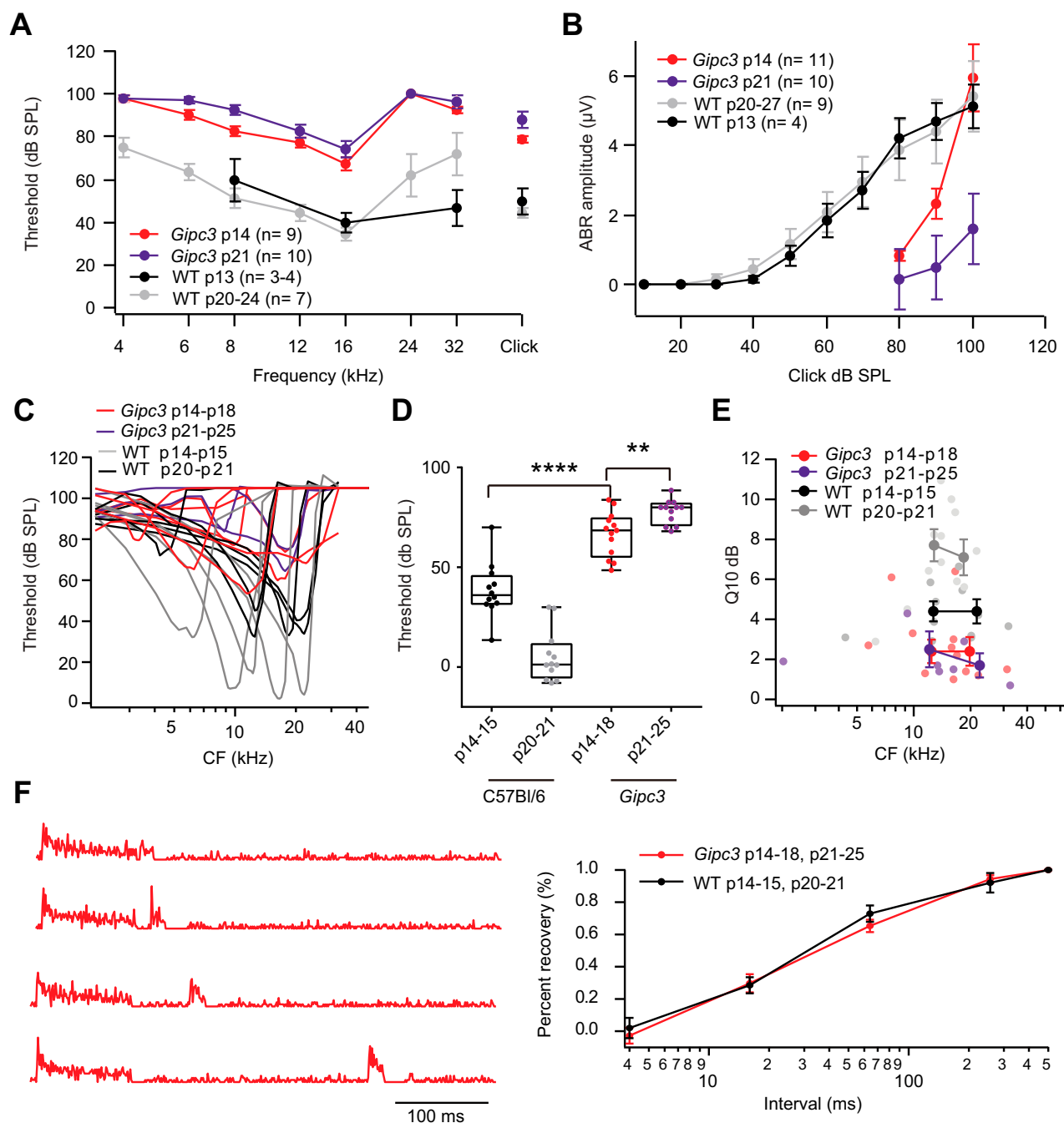


Fig. S5. Genetic disruption of harmonin function leads to decreased ribbon size and hyperpolarizing shift of the activation of Ca^{2+} influx but leaves developmental confinement of Ca^{2+} and expression of large-conductance Ca^{2+} -activated K^+ channels unaltered. (A) Distribution of the intensities of AZ TAMRA-peptide fluorescence in *dfcr* (red, 105 AZs of 15 IHCs, c.v. = 0.26) and in WT (BALB/c, black, 107 AZs of 14 IHCs, c.v. = 0.35) IHCs (Left) and box plot (Right) depicting a significant decrease in the fluorescence intensity of labeled ribbons in *dfcr* IHCs (Left, $P < 0.05$, Wilcoxon rank sum test). (B) Fractional activation of AZ Ca^{2+} influx shows comparable heterogeneity of *dfcr* (red) and WT (black) IHCs, but a more hyperpolarized mean $V_{0.5}$ in *dfcr* IHCs (Right, $P < 0.05$, t test). Experiments were performed as in Fig. 3. Thin lines present the fractional activation of individual AZs of *dfcr* (light red, 105 synapses) and WT (gray, 107 synapses) and thick red and black lines the mean fractional activation, respectively. (C) Fractional activation of the whole-cell Ca^{2+} conductance (GCa). (Left) The activation of single IHCs (thinner and lighter traces) from *dfcr* (red and light red, 14 IHCs) and WT (black and gray, 15 IHCs) and mean fractional activation of all IHCs (thick and dark traces), respectively. In agreement with the single AZ data (B), the mean $V_{0.5}$ of the whole-cell Ca^{2+} conductance was also shifted toward more hyperpolarized potentials in the *dfcr* cells (Right, $P < 0.05$, Wilcoxon rank sum test). (D) Current-voltage relationship for I_{Ca} evoked by 20-ms voltage steps in whole-cell patch-clamp recordings from *dfcr* (red, 14 IHCs) and WT (black, 15 IHCs) cells showing an increased Ca^{2+} current peak in the *dfcr* mice (Left, mean \pm SEM, $P < 0.05$, Wilcoxon rank sum test). However, the maximal AZ Ca^{2+} influx *dfcr* (red, 105 AZs, c.v. = 0.61) was not significantly different from that of WT (black, 107 AZs, c.v. = 0.83), suggesting an increased extrasynaptic Ca^{2+} influx (Right). (E) Maximum projection of confocal sections of organs of Corti immunolabeled for $\text{Ca}_v1.3$ (green) and RIBEYE/CtBP2 (red). Most $\text{Ca}_v1.3$ immunofluorescence was confined to presynaptic AZs (labeled by the RIBEYE immunofluorescence) in both *dfcr* (Right) and WT (Left) IHCs. Immaturity would have expected to cause a lack of BK immunofluorescence. (Scale bar: 10 μm .)



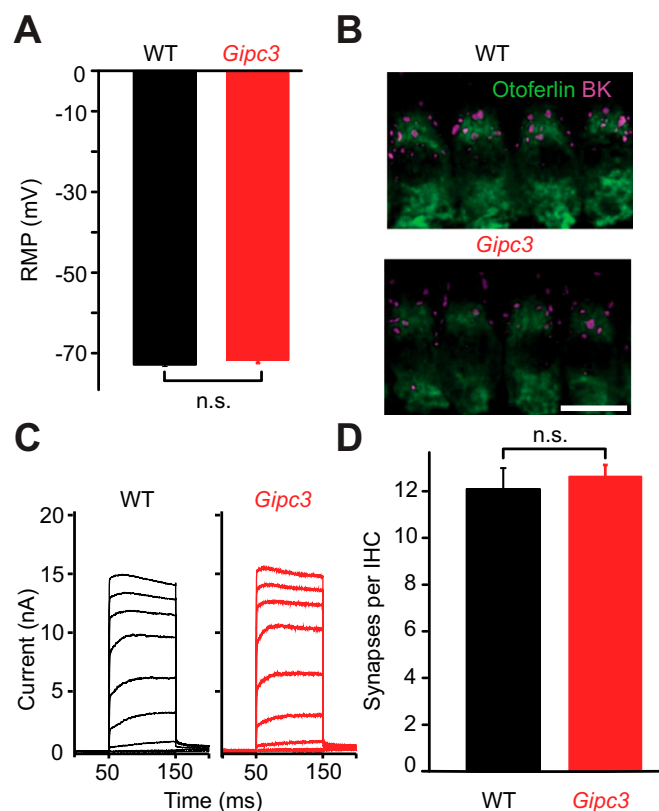


Fig. S7. Increased whole-cell Ca^{2+} current but largely maintained IHC K^{+} currents and synapses in IHCs of *Gipc3* mutant mice. (A) The resting membrane potential as recorded in the current-clamp configuration was normal in *Gipc3* mutant IHCs: 71.7 ± 0.7 mV, $n = 12$ for *Gipc3* mutant IHCs vs. -72.8 ± 0.5 mV; $n = 19$, for WT IHCs ($P = 0.21$, both p14–16). (B) Maximum projection of confocal section of immunolabeled organs of Corti: *Gipc3* mutant IHCs (visualized by otoferlin immunofluorescence) show clusters of large-conductance Ca^{2+} -activated K^{+} channels (magenta) at their “neck” region. (C) Representative potassium currents in *Gipc3* mutant and WT IHCs: no obvious reduction due to *Gipc3* disruption. (D) Normal number of ribbon synapses in *Gipc3* mutant IHCs of 2-wk-old mice (12.09 ± 0.9 , $n = 28$ for WT, 12.6 ± 0.5 , $n = 44$ for *Gipc3*, $P = 0.48$). Analysis was performed on confocal stacks of organs of Corti following immunolabeling for RIBEYE/CtBP2 and postsynaptic GluA2/3.